Atmos. Chem. Phys. Discuss., 15, 7895–7932, 2015
www.atmos-chem-phys-discuss.net/15/7895/2015/
doi:10.5194/acpd-15-7895-2015
© Author(s) 2015. CC Attribution 3.0 License.

Atmospheric Chemistry and Physics Discussions
Open Access

This discussion paper is/has been under review for the journal Atmospheric Chemistry and Physics (ACP). Please refer to the corresponding final paper in ACP if available.

Transport of Antarctic stratospheric strongly dehydrated air into the troposphere observed during the HALO-ESMVal campaign 2012

C. Rolf[1], A. Afchine[1], H. Bozem[2], B. Buchholz[3], V. Ebert[3], T. Guggenmoser[1,*], P. Hoor[2], P. Konopka[1], E. Kretschmer[4], S. Müller[2], H. Schlager[5], N. Spelten[1], O. Sumińska-Ebersoldt[4], J. Ungermann[1], A. Zahn[4], and M. Krämer[1]

[1]Forschungszentrum Jülich, IEK-7, 52457 Jülich, Germany
[2]Institute for Atmospheric Physics, Johannes Gutenberg University of Mainz, 55122 Mainz, Germany
[3]Physikalisch-Technische Bundesanstalt (PTB), 38116 Braunschweig, Germany
[4]Karlsruher Institut für Technologie (KIT), IMK-ASF, 76021 Karlsruhe, Germany
[5]Deutsches Zentrum für Luft und Raumfahrt, IPA, 82234 Oberpfaffenhofen, Germany
[*]now at: European Space Agency, Noordwijk, the Netherlands

Received: 13 February 2015 – Accepted: 25 February 2015 – Published: 16 March 2015

Correspondence to: C. Rolf (c.rolf@fz-juelich.de)

Published by Copernicus Publications on behalf of the European Geosciences Union.

CC BY

Abstract

Dehydration in the Antarctic winter stratosphere is a well-known phenomenon that is occasionally observed by balloon-borne and satellite measurements. However, in-situ measurements of dehydration in the Antarctic vortex are very rare. Here, we present detailed observations with the in-situ and GLORIA remote sensing instrument payload aboard the new German aircraft HALO. Strongly dehydrated air masses down to 1.6 ppmv of water vapor were observed as far north as 47° S and between 12 and 13 km in altitude, which has never been observed by satellites. The dehydration can be traced back to individual ice formation events, where ice crystals sedimented out and water vapor was irreversibly removed. Within these dehydrated stratospheric air masses, filaments of moister air reaching down to the tropopause are detected with the high resolution limb sounder, GLORIA. Furthermore, dehydrated air masses are observed with GLORIA in the Antarctic troposphere down to 7 km. With the help of a backward trajectory analysis, a tropospheric origin of the moist filaments in the vortex can be identified, while the dry air masses in the troposphere have stratospheric origins. The transport pathways of Antarctic stratosphere/troposphere exchange are investigated and the irrelevant role of the Antarctic thermal tropopause as a transport barrier is confirmed. Further, it is shown that the exchange process can be attributed to several successive Rossby wave events in combination with an isentropic interchange of air masses across the weak tropopause and subsequent subsidence due to radiative cooling. Once transported to the troposphere, air masses with stratospheric origin are able to reach near-surface levels within 1–2 months.

1 Introduction

Antarctic stratospheric dehydration occurs regularly every winter and spring in the very isolated southern hemispheric polar vortex (e.g. Vömel et al., 1995; Kelly et al., 1989; Schoeberl et al., 1992; Nedoluha et al., 2002; Jimenez et al., 2006). The reason is that

ACPD
15, 7895–7932, 2015

CC BY

the temperatures in the Antarctic stratosphere are sufficiently low for ice particles to form. These ice particles may sediment depending on their size and thus transport water to lower altitudes. If dehydration extend down to the tropopause, water is removed from the stratosphere and changing the water vapor budget of the lower Antarctic vortex drastically. After the break-up of the Antarctic vortex, redistribution and exchange between vortex air and air masses outside the vortex lead to a return to typical background water vapor mixing ratios which lie around 4–5 ppmv (Nedoluha et al., 2007). Rehydration with redistribution of water from the solid into the gas-phase occurs at lower altitudes where ice crystals sublimate caused by a temperature increase. Additionally, sedimenting ice crystals can take up nitric acid and cause denitrification, which can strengthen and prolong the ozone depletion in polar regions (Solomon, 1999; Khosrawi et al., 2011). In the Arctic region, stratospheric dehydration is also possible but much less frequent than in the Southern Hemisphere (e.g. Schiller et al., 2002; Khaykin et al., 2013).

Dehydration of vortex air masses is observed frequently by satellite measurements (e.g. Nedoluha et al., 2002; Jimenez et al., 2006; Schoeberl and Dessler, 2011). However, satellite measurements in the lower stratosphere and upper troposphere (UT/LS) do not offer the necessary horizontal and vertical resolution to be suitable for process studies in the tropopause region. Balloon borne measurements launched from the Antarctic continent also observed dehydration and the corresponding rehydration (e.g. Vömel et al., 1995). Beside these balloon soundings, only three aircraft campaigns have been conducted where Antarctic stratospheric air masses were probed in-situ; two US campaigns with the ER-2 aircraft (AAOE in 1987; Tuck et al., 1989, and ASHOE in 1994; Tuck et al., 1997) and one European campaign with the Geophysica aircraft (APE-GAIA in 1999; Giovanelli et al., 2005). In-situ measurements in the Antarctic vortex are very rare, since the flight range of research aircraft is limited. This paper focuses on one measurement flight directly into the Antarctic vortex that was performed as part of the ESMVal (Earth System Model Validation; Schlager, 2014) campaign in September 2012 with the new German research aircraft HALO (High Altitude

ACPD
15, 7895–7932, 2015

CC BY

and LOng range; Krautstrunk and Giez, 2012). The ESMVal campaign was embedded in the TACTS (Transport And Composition in the Upper Troposphere/Lowermost Stratosphere; Engel et al., 2013) campaign which took place just before and after the ESMVal flights in August and the end of September 2012. A mutual scientific objective of both campaigns was to investigate the transition region between the troposphere and stratosphere. Here, we want to note that HALO was equipped with in-situ instruments as well as the high resolution limb sounder, GLORIA (Gimballed Limb Observer for Radiance Imaging of the Atmosphere). This combination of high-precision in-situ measurements together with sophisticated remote sensing observations in the UT/LS is an outstanding attribute of both campaigns. Another objective of the ESMVal flights was to get a full meridional cross section of atmospheric measurements for global chemistry model evaluation. Hence, the Antarctica flight was performed in an effort to get as far south as possible and reach the stratospheric vortex. During this flight, dehydrated air masses were measured in-situ quite far north up to 45° S between 12 and 13 km. In contrast, Aura-MLS and POAM 3 satellite measurements (Nedoluha et al., 2002; Jimenez et al., 2006; Schoeberl and Dessler, 2011) do not show dehydrated air masses as far north (not beyond 57° S) and as low in the stratosphere and upper troposphere as was observed during this ESMVal flight.

In general, the process of dehydration is well understood. Relatively less is known about the fate of the dehydrated air masses. The air within the Antarctic polar vortex is highly isolated with a weak exchange of trace gases across the vortex edge driven by stratospheric planetary Rossby waves propagating from the troposphere and Rossby wave breaking (RWB) events. However, these mainly disturb the bottom of the polar vortex. Normally, the vortex edge in the Southern Hemisphere is less strongly disturbed than in the Arctic due to less wave activity (Schoeberl et al., 1992). In the Arctic and in midlatitudes, intrusion of stratospheric air into the troposphere seems to occur more frequent and was discussed by Khosrawi et al. (2006) where at the edge of the deep intrusion dehydration was observed. Nevertheless, Antarctic stratospheric air masses can be vertically transported through the thermal tropopause directly into

ACPD
15, 7895–7932, 2015

CC BY

the troposphere and dry the troposphere down to the Earth's surface. In addition, this air is mostly rich in ozone and reactive nitrogen due to the stratospheric origin and can influence the chemical composition of the Antarctic troposphere (Stohl and Sodemann, 2010; Mihalikova and Kirkwood, 2013). Stohl and Sodemann (2010) identify two general processes that transport stratospheric air masses down to near-surface levels. The first process consists of katabatic winds over the Antarctic Plateau caused by the high topography that create a general downwelling above the Antarctic continent as reported by Roscoe (2004). The second process is driven by mid-latitude cyclones on the poleward side of the jet stream that support RWB events and a corresponding stratospheric intrusion as reported by Ndarana et al. (2012). Rossby wave induced stratospheric intrusions, such as tropopause folds, occur more often further north and in the midlatitudes than directly above the Antarctic continent (James et al., 2003). Once an airmass is in the troposphere, the mean cooling rates cause a reduction in potential temperature and the airmass will descend from the tropopause to near-surface heights within 10 days (descent rate of 5 $mm\,s^{-1}$) as reported by van de Berg et al. (2007). However, the frequency, the seasonality, and the process behind tropopause folds and stratospheric intrusions in the Antarctic region is still under debate (Stohl and Sodemann, 2010; Ndarana et al., 2012; Mihalikova and Kirkwood, 2013).

The study presented here is structured as follows: in Sect. 2, a brief overview of the different instruments and data used is given. The in-situ and remote sensing measurements across the Antarctic polar vortex are described in Sect. 3, where it is also shown that dehydration occurs directly in the transition region between the upper troposphere and lower stratosphere (UT/LS). Furthermore, Sect. 4 includes a case study of observed stratosphere/troposphere exchange of dehydrated air masses combined with an extensive trajectory analysis showing how deep below the thermal tropopause dehydrated air masses can be found.

ACPD
15, 7895–7932, 2015

CC BY

2 Instrumentation and meteorological data

The new German research aircraft, HALO, deployed during TACTS and ESMVal has a long flight endurance of up to 12 h. This enables air masses in the Antarctic vortex to be sampled without landing in Antartica. Altogether, a set of nine in-situ instruments for measuring trace gases and one remote sensing instrument were installed aboard HALO. For the study presented here, we use the water vapor data of FISH and HAI as well as measurements from TRIHOP for methane and FAIRO for ozone. The remote sensing instrument, GLORIA, provides cross-sections of trace gases that are fairly parallel to the flight track of the aircraft. GLORIA's high vertical resolution makes it particularly suited for the investigation of small-scale structures.

In addition to the aircraft measurements, satellite observations from CALIPSO and meteorological data from ECMWF are used for further interpretation of the observed situation. The instruments and meteorological data are described in the following subsections.

2.1 FISH – total water measurements (in-situ H_2O)

The airborne Lyman-α photofragment fluorescence hygrometer FISH (Fast In-situ Stratospheric hygrometer) is a well-established closed-path instrument for measuring water vapor in the range of 1 to 1000 ppmv (Zöger et al., 1999). The FISH is especially built to measure the low water vapor mixing ratios prevailing in the upper troposphere and lower stratosphere. It is regularly calibrated on the ground to a reference frost point hygrometer (MBW DP30) and had an accuracy of 6 % ± 0.4 ppmv during TACTS and ESMVal campaigns (Meyer et al., 2015). The air supply for the measuring cell is provided by a forward facing inlet, which also samples ice crystals if present (H_2O_{cond}). Together, the evaporated crystals and the gas-phase water (H_2O_{gas}) sum up to a total water measurement.

ACPD
15, 7895–7932, 2015

cc BY

2.2 HAI – total water measurements (in-situ H_2O)

The novel Hygrometer for Atmospheric Investigation (HAI) (Buchholz, 2014) is a fast, airborne, in-situ hygrometer capable of multi-phase water detection that employs direct Tunable Diode Laser Absorption Spectroscopy (dTDLAS) in combination with a special data retrieval method, which allows absolute water vapor measurements without any sensor calibration (Buchholz et al., 2013). This data retrieval was recently successfully validated via a direct side by side comparison with the German metrological water vapor scale (Buchholz et al., 2014). HAI is a 2 × 2, multi-channel TDLAS spectrometer which realizes, in a unique concept, a simultaneous gas phase and total water measurement via a parallel water detection in an open-path cell, outside the aircraft fuselage, and in extractive (i.e. gas sampling) closed-path cells inside the aircraft. To enlarge the dynamic range to 1–40 000 ppmv, both cell types are simultaneously probed by two laser wavelengths, at 1.4 µm for the lower to mid troposphere and at 2.6 µm for the upper troposphere and the stratosphere. The ranges of the 1.4 and 2.6 µm spectrometer channels overlap and therefore provide a redundant, independent detection between 10 and about 5000 ppmv. The metrologically calculated spectrometer uncertainties are 4.3 % ± 3 ppmv at 1.4 µm and 5.9 % ± 0.4 ppmv at 2.6 µm. In this study, data from the two closed-path spectrometers are used, i.e. total water measurements similar to FISH.

2.3 TRIHOP – methane measurement (in-situ CH_4)

The TRIHOP instrument is a three channel Quantum Cascade Laser Infrared Absorption spectrometer capable of the subsequent measurement of CO, CO_2, N_2O and CH_4. During TACTS/ESMVal the instrument was calibrated in-situ against secondary standards of compressed ambient air which are traceable against NOAA standards. Integration time for each species was 1.5 s at a duty cycle of 8 s, which finally limits the temporal resolution of the measurements. For the ESMVal flight on 13 Septem-

ACPD
15, 7895–7932, 2015

CC BY

ber 2012, TRIHOP CH4-data achieved a precision (2σ) of 9.5 ppbv and accuracy of 13.5 ppbv, respectively, without any corrections applied.

2.4 FAIRO – ozone measurement (in-situ O_3)

FAIRO is a new accurate ozone instrument developed for use on board the HALO aircraft. It combines two techniques, the UV photometry (light absorption of O_3 at λ = 250–260 nm) with high accuracy and chemiluminescence detection with high measurement frequency. A UV-LED is used as a light source for the UV photometer, which can be controlled well (in contrast to Hg lamps) for constant light emission. The 1-sigma precision is 0.08 ppbv at a measurement frequency of 4 s and a cuvette pressure of 1 bar and the total uncertainty is 2 %. The chemiluminescence detector shows a measurement frequency of 12.5 Hz and a high precision of 0.05 ppbv (at 10 ppbv absolute, a measurement frequency of 5 Hz, and a pressure of 1 bar) (Zahn et al., 2012).

2.5 GLORIA (aircraft remote sensing)

The Gimballed Limb Observer for Radiance Imaging of the Atmosphere (GLORIA) combines a two-dimensional focal plane detector array with a Fourier-transform spectrometer to capture about 6000 infrared limb spectra simultaneously. This enables remote sensing observations with high vertical and horizontal resolution to resolve small scale structures (see Riese et al., 2014). The spectral sampling can be switched between 0.625 and 0.0625 cm^{-1} at the cost of an increased acquisition time in case of higher spectral resolution (Friedl-Vallon et al., 2014). The gimbal mount and inertial altitude control system allows GLORIA to maintain a steady pointing on a moving aircraft; it can also be used to point the instrument at a range of azimuth angles with respect to the aircraft, covering about 70°. This allows for tomographic measurement patterns and 3-D reconstruction of fine-scale filamentary structures (Ungermann et al., 2011; Kaufmann et al., 2014). The vertical location of retrieved quantities approximately follows the tangent points of the measurement geometry (parabola curve through the

ACPD
15, 7895–7932, 2015

CC BY

atmosphere). Thus, while the location of quantities retrieved at flight level lies in the vicinity of the aircraft, the locations of quantities at lower altitudes are several tens to hundreds of kilometers away. Concerning the water vapor product used in this paper, Ungermann et al. (2014) showed that GLORIA water vapor at flight level agrees fairly well with the in-situ FISH measurements, within error bars. The deviations to FISH during the ESMVal/TACTS flights are mostly less than 0.4 ppmv.

2.6 CALIPSO (satellite remote sensing)

The Cloud-Aerosol Lidar and Infrared Pathfinder Satellite Observation (CALIPSO) satellite is one of five satellites in the NASA A-train constellation. CALIPSO completes 14.55 orbits per day with an inclination of 98.2° and thus delivers good coverage above the polar regions. Besides one wide field camera and an imaging infrared radiometer, the Cloud-Aerosol Lidar with Orthogonal Polarization (CALIOP) is aboard CALIPSO. The lidar operates with two wavelengths (532, 1064 nm) with additional polarization-sensitivity, providing high-resolution vertical backscatter profiles of aerosols and clouds. In this study we use the CALIPSO Lidar Level 2 Polar Stratospheric Cloud (PSC) data product, which is described in Pitts et al. (2009) and Pitts et al. (2011). This data product provides a PSC composition scheme on a daily basis for all nighttime orbits with a resolution of 5 km horizontally by 180 m vertically.

2.7 ECMWF (meteorological data)

Global meteorological reanalysis ERA-Interim data (Dee et al., 2011) of the ECMWF (European Centre for Medium-Range Weather Forecasts) are used to facilitate the interpretation of the observations. The meteorological fields have a resolution of $1^{\circ} \times 1^{\circ}$ with 60 vertical levels from the surface (1000 hPa) up to 0.1 hPa. Every 6 h a full global dataset is available. The trajectories used in Sect. 4 are based on the horizontal wind fields and diabatic heating rates; additional parameters like temperature, pressure etc. are added to the trajectories from the ERA-Interim data.

ACPD
15, 7895–7932, 2015

3 ESMVal flight on 13 September 2012

3.1 Meteorological situation/flight pattern

The ESMVal flight on 13 September 2012 was performed from Cape Town (South Africa) heading towards Antarctica until 65° S at an altitude of 12–13 km (see Fig. 1). After a dive from 12.5 km down to 3 km to sample the transition from the polar stratosphere to the troposphere, the return flight took place at 12.5 km and rose up to 15 km shortly before descending back to Cape Town. A hexagonal flight pattern was included in the flight path back to Cape Town to enable the tomographic study of trace gases with GLORIA. The ECMWF wind field (black lines) as well as the strongly increasing potential vorticity (PV, see Fig. 2) show that the vortex edge (yellow dots) was far north, up to 47° S. The vortex edge is determined according to the definition of Nash et al. (1996). The color code in Fig. 1a represents the in-situ measured water vapor mixing ratios from FISH along the flight path. Directly south of the vortex edge the water vapor mixing ratios decrease rapidly to below 2.5 ppmv (purple dots along the flight path).

The latitudinal cross section of equivalent latitude (calculated from the ECMWF PV field) along the flight path is shown in Fig. 1b. The thermal tropopause (light blue dots) stays almost constant at around 10 km and rises up to 12 km further poleward. The PV and equivalent latitude are nearly conserved with time in the stratosphere but less strongly so in the troposphere due to small scale mixing. The equivalent latitude shows high values within the vortex and thus marks clearly the vortex air masses. However, high equivalent latitudes of 70–80° S show up far below the thermal tropopause down to 5 km altitude in the latitude range from 60–45° S. This indicates that these air masses originate from higher latitudes and were transported from the stratosphere through the thermal tropopause. The transport process can be shown and confirmed with the trajectory analysis in Sect. 4.2. Interestingly, the 310 K isentrope crosses the thermal tropopause once (65° S) and the 320 K isentrope crosses it three times (58, 55 and 50° S) on the poleward side of the jet core. Therefore, air masses can be potentially transported from the stratosphere into the troposphere and vice versa. The flight path

ACPD
15, 7895–7932, 2015

CC BY

crosses the air masses with high equivalent latitude in the stratosphere before and after the dive. The dive down to 3.5 km altitude was performed on the poleward side of the high equivalent latitude tropospheric air masses.

3.2 Observations

The time series of the in-situ measurements are shown in Fig. 2, where the measurements of the water vapor instruments are visible in the upper panel and the measurements of the tracers for defining stratospheric/vortex air masses are shown in the lower panel. After the ascent of HALO near Cape Town, the water vapor mixing ratio decreases to the typical stratospheric value of 4 ppmv, from 06:30 until 08:15 UTC. During this time, ozone and PV (i.e. the stratospheric tracers with low values in the troposphere) show an increase compared to the values before 06:30 UTC, while methane (tropospheric tracer with low values in the stratosphere) shows a slight decrease from 1790 to 1740 ppbv. Both indicates that the aircraft entered the stratosphere. Henceforth, methane and water vapor further decrease to 1650 ppbv and 3 ppmv respectively on the same flight level starting at 08:15 UTC, and simultaneously ozone and PV further increase. This is the time when HALO penetrated the Antarctic vortex (marked in blue in Fig. 2). After ascending to a higher flight level (08:35 UTC), water vapor decreases to slightly above 2 ppmv and stays there until the southernmost point was reached and the dive started at 11:00 UTC. This low water vapor in the time between 08:15 and 11:00 UTC coincides well with high equivalent latitude (see Fig. 1b). Subsequently, the strong increase in methane and decrease in ozone and PV indicate the penetration of the aircraft into the Antarctic troposphere at 11:00 UTC. After returning to the previous flight level (11:45 UTC), the vortex signatures with low values of water vapor and methane as well as high values of ozone and PV show up again. However, at this point ($\sim$ 12:30 UTC) the water vapor mixing ratio reaches the lowest value of 1.6 ± 0.5 ppmv together with a strong maximum in ozone and PV. The low water vapor below 4 and even below 2 ppmv indicates strongly dehydrated air masses.

ACPD
15, 7895–7932, 2015

The saturation mixing ratio with respect to ice within the vortex is three to four times larger than the measured water vapor mixing ratio. Thus, the sampled air masses were clearly sub-saturated with relative humidities of 25–33 % and it is unlikely that ice particles remained in the probed air masses. In addition, HAI and FISH show no peaks in the total water vapor time series (based on 1 Hz data), which would indicate the presence of ice particles on the flight level. Especially, the water vapor mixing ratios around 2 ppmv during the stratospheric flight legs (06:30 to 11:00 and 11:45 to 15:45 UTC) are very smooth and show no significant variations. Thus, both water vapor instruments, FISH and HAI, measured only gas-phase water vapor, and no cloud particles were present in the vortex air. Both FISH and HAI observed these low water vapor mixing ratios independently.

In order to show the fairly good agreement of both water vapor instruments FISH and HAI based on 1 Hz data at the observed low water vapor values, we choose two flight legs for the comparison (leg one: 09:45–10:45 UTC and leg two: 13:00–14:00 UTC). During flight leg one, both hygrometers have an absolute difference of 0.21 ppmv and a mean relative difference of −14.9 % (±10.5 %, 1σ). During flight leg two, a difference of 0.26 ppmv and a mean relative difference of −5.9 % (±7.3 %, 1σ) is found. These rather small differences are consistent with the uncertainties of both hygrometers, which are ±0.45 and ±0.5 ppmv at the 2 ppmv level for FISH and HAI, respectively. The HAI data measured before 09:10 UTC (marked with gray in Fig. 2) are influenced by an untypical memory effect of the measurement cell during ascent, caused by a valve which was opened too late, but only when flying in the upper troposphere. As a result, the "wet" measurement cells were not sufficiently dried off with the high mass flows during take-off and ascent. This also explains the asymmetry in the deviations to FISH before and after the dive. In addition, the agreement of GLORIA water vapor observations at flight level with the two in-situ instruments, FISH and HAI, is remarkably good, considering that GLORIA is a remote sensing instrument.

The GLORIA instrument measures quasi-vertical profiles along the flight path by viewing the atmosphere on the right side of HALO. Here, we focus on the H_2O re-

ACPD
15, 7895–7932, 2015

CC BY

trieval product, which is shown in Fig. 3. We consider only the times from 08:00 to 14:00 UTC to focus on the air masses where GLORIA observed vortex air (the whole dataset is from 06:30 to 15:30 UTC). The dive is noticeable as the white area between 11:00 and 12:00 UTC, where GLORIA did not measure in order to prevent condensation of tropospheric water vapor on the cold instrument. The dry vortex air masses are clearly visible between 08:00 and 13:00 UTC at flight level (black solid line in Fig. 3), but also below, down to altitudes of 7 km. As mentioned in Sect. 2.5, the quantities retrieved from GLORIA are approximately placed on a parabola following the tangent points through the atmosphere (e.g. 250 km horizontal distance to flight path at 9 km altitude). The dry region just before the dive was measured by GLORIA in the westerly direction to the flight path on the way towards Antarctica, while the air masses after the dive are measured in the easterly direction on the way back to Cape Town. Thus, the dehydrated air masses below the thermal tropopause seem to cover a large region, having a dimension of at least 500 km horizontally at 9 km altitude.

The thermal tropopause is also derived from the GLORIA retrieved temperature profiles and is marked with black dots. Interestingly, low water vapor mixing ratios around and below 2 ppmv are observed beneath the thermal tropopause. Especially in the time range from 09:00 to 10:30 UTC and from 12:00 to 13:30 UTC, very dry air masses with water vapor mixing ratios of 2–3 ppmv can be found far below the thermal tropopause, down to 7 km. This indicates that dehydrated stratospheric air masses could have been transported through the thermal tropopause into the troposphere. The dynamic tropopause, which is between the −4 and −2 PVU isoline, is somewhat lower than the thermal tropopause at ~ 7 km in the time range from 12:00 to 13:30 UTC and indicates a proceeding stratospheric intrusion. In Sect. 4.2, we analyze this transport process with the help of airmass backward trajectories. In addition, no water vapor values less than 6 ppmv are found below the −4 PVU isoline in ECMWF data (not shown here). This shows, at least for this situation, that the transport process of dry stratospheric air masses into the troposphere is not captured by the ECMWF meteorological analysis (see Sect. 4).

ACPD
15, 7895–7932, 2015

CC BY

Embedded in the dry vortex air masses, small filaments (marked in Fig. 3 with red boxes) of enhanced water vapor are visible. These filaments may indicate rehydration layers, where sedimented ice particles from upper layers have sublimated and resulted in layers of enhanced water vapor as described in Khaykin et al. (e.g. 2013) for the Arctic. However, trajectory reverse domain filling (RDF) (Sect. 4.2) showed that these air masses could not be attributed to rehydration. Also the in-situ measurements of FISH/HAI showed no evidence of a rehydration layer during the dive from ∼ 12.5 to 3 km and back. We have analyzed these somewhat moister air masses in more detail, as discussed in the next section.

4 Trajectory based case study of 13 September 2012

Detailed investigation of the observed Antarctic dehydration is performed using air-mass trajectories calculated with the tool CLaMS-traj which is part of the Chemical Lagrangian Model for the Stratosphere (CLaMS) (McKenna et al., 2002; Konopka et al., 2007). The trajectories are driven by the ERA-Interim reanalysis horizontal winds and diabatic heating rates (Dee et al., 2011; Ploeger et al., 2010). Besides temperature, pressure, and humidity along the trajectories, the potential vorticity (PV) and thermal tropopause height (WMO lapse rate criterion) are added from the ECMWF meteorological fields. The temperatures from ECMWF along the flight path agree very well with the measured temperatures from the HALO aircraft (not shown here). The mean deviation on each flight level is mostly around 0.4 K, and the temperatures in ECMWF are slightly lower than the measured temperatures.

4.1 History of dehydrated air masses along flight path

In this section, we investigate the history of the in-situ measured dehydrated air masses. For that purpose, the trajectories are calculated every 10 s along the flight path, each reaching 50 days backwards in time. For further analysis, we selected all

ACPD
15, 7895–7932, 2015

CC BY

trajectories between 12:20–12:29 UTC (in total 54), where the lowest water vapor mixing ratios were measured. However, the other trajectories with measured low water vapor mixing ratios between 2 and 3 ppmv show very similar history. Figure 4 shows the median saturation mixing ratio with respect to ice (orange line) and the frequency distribution (gray scale color-code) of every 1 h trajectory time step of all trajectories calculated by ClaMS along the 50 days back in time. The trajectories show the same history in saturation mixing ratio from 13 September until 14 August, where the gray colors start to spread out. This indicates that the trajectories have the same path with the same temperature history for at least 30 days. After this time, the trajectories split up into two branches, indicating a bifurcation point and associated mixing on 14 August. The trajectories within the branch with lower saturation mixing ratios of 2 to 3 ppmv below the median line stay together on the same path until the beginning of August. The trajectories before the 1 August have different saturation mixing ratios indicating the dispersion of air masses, which limits the interpretation of the trajectory calculations.

To show the presence of ice particles and subsequent dehydration, CALIPSO data (see Sect. 2.6) are used. A distance criterion is used to match the airmass trajectories with the CALIPSO data. Every trajectory at a specific time which coincides with the CALIPSO orbit inside a square of ±5° latitude and ±5° longitude is checked for the presence of ice in an altitude range of ±0.2 km. If more than 50 % of all trajectories at one time coincide with a CALIPSO ice observation, the corresponding time periods are marked with a blue bar (see Fig. 4).

Figure 4 illustrates the coincidence of low saturation mixing ratios along the trajectories with observed ice formation (CALIPSO) in the considered air masses. The trajectories pass several cold regions associated with low saturation mixing ratio where ice formation is initiated. If the ice cloud and supersaturation exist long enough (typically around 0.5–1 day, Nedoluha et al., 2002) to allow the ice particles to grow to sizes of several microns (diameter of 10 to 20 µm), sedimentation of these ice particles begins and causes irreversible dehydration. The sedimented ice particles with these sizes fall with velocities of around 2.5 km d^{-1} (see Müller and Peter, 1992) until warmer

ACPD
15, 7895–7932, 2015

CC BY

temperatures in lower regions causes them to evaporate. With each pass of a cold region, more and more water vapor is removed from the airmass. As stated by Nedoluha et al. (2002), air masses must undergo several periods with dehydration before reaching the 1 to 2 ppmv mixing ratio level, which is typically observed by satellites within the vortex in the Antarctic spring. This periodic behavior is confirmed by Fig. 4, where trajectories undergo four events with low saturation mixing ratios and simultaneous ice cloud observations by CALIPSO. The first and the second period (1 and 9 August) reveal rather high saturation mixing ratios of around 3 ppmv. In every later period, colder temperatures and lower saturation mixing ratios are necessary to initiate additional ice formation and dehydration. So the third and the fourth period on 16 and 29 August where CALIPSO observed ice show lower saturation mixing ratios of 1.5 and 1.2 ppmv, respectively. The last two events will have dried out the air masses to the final state of about 1.6 ppmv, which is observed by the FISH and HAI instruments. After this strong dehydration, the temperatures became warmer in the late Antarctic spring and summer and no additional dehydration took place according to the simulations.

The recurring low saturation mixing ratios and corresponding low temperatures are primarily caused by gravity waves, which are induced by the high topography of the Antarctic continent (Stohl and Sodemann, 2010). Especially, the first three ice formation events occurred just as the trajectories passed the Antarctic Peninsula (northernmost part), which is a strong source of gravity waves (e.g. Ern et al., 2011; Hoffmann et al., 2013). Only the last freezing event with the lowest supersaturation occurs above the Antarctic Plateau (central part) in the north-east of the continent.

After freezing, the ice particles can even reach the troposphere due to sedimentation, especially if dehydration takes place at low altitudes (11.5–12.5 km) as observed during the Antarctic ESMVal flight with HALO. The lack of rehydration signatures in the GLORIA measurements (see Fig. 3) also indicates the permanent removal of water vapor from the stratosphere, as will be further discussed in Sect. 4.2. The air masses from which the ice particles originate and the air masses where they sublimate behave very differently in dynamical perspective. Due to the length of time since the last

ACPD
15, 7895–7932, 2015

cc BY

dehydration on 28 August (16 days before measurement) it is very unlikely that rehydrated air masses would still be found below the observed dehydrated air masses in the troposphere. In addition, the in-situ measurements taken during the dive confirm the absence of any observed rehydration features.

4.2 History of air masses observed by GLORIA

The trajectories for analyzing the transport of dehydrated air masses observed by GLORIA are calculated 150 days backward in time from each tangent point (in total 30 000 single trajectories). In addition, the trajectories are also calculated 30 days forward to show where the air masses are further transported. With this set of trajectories, the GLORIA measurements can be interpreted and the associated transport pathways can be investigated.

4.2.1 Vortex air masses

From the in-situ ozone and methane measurements, it is visible that the HALO aircraft has penetrated the Antarctic vortex (see Sect. 3.2). The identification of vortex air masses in the GLORIA trace gas cross-sections is performed using the tangent point trajectories. Figure 5 shows the amount of time that the trajectory for each GLORIA tangent point stayed within the vortex before the measurement took place. To calculate this so-called vortex indicator, the vortex border needs to be determined at each trajectory time step with the Nash criterion (Nash et al., 1996). Then, the time that each individual trajectory remains within the vortex border is counted backwards from the time of measurement. This procedure is limited to the preceding 50 days. The blue color in Fig. 5 shows the trajectories that stay in the vortex for at least the last 50 days. In contrast, air masses that were never in the vortex are indicated by a deep red color. This includes tropospheric air, but also stratospheric air masses north of 48° S. Interestingly, a sharp boundary between deep red and deep blue colors appears between 09:00 and 11:00 UTC and also between 11:45 and 12:20 UTC, which exactly follows

ACPD
15, 7895–7932, 2015

cc BY

the measured thermal tropopause (black dots). Here, the fundamental role of the thermal tropopause as a vertical transport barrier for stratosphere/troposphere exchange emerges.

In contrast, the air masses that spent between 5 and 40 days in the vortex (marked by light blue and reddish colors) indicate mixing of outside air into the vortex. Even at the vortex edge and in the core of the vortex itself, small filaments are apparent. As indicated in Sect. 3.2, some filaments with elevated amounts of water vapor were also observed with GLORIA. Two of these filaments observed around 13:00 UTC between 10 to 12 km altitude can be found with this Nash PV criterion showing vortex residence times of 5 days (filament 6) and 35 days (filament 7), respectively. This shows that these filaments are likely freshly mixed in from outside the vortex and thus could potentially contain higher water vapor content compared to the dehydrated vortex air and therefore weaken the hypothesis of rehydration signatures.

To show that all observed filaments (red boxes in Fig. 3) are caused by mixing, reverse domain filling (RDF) is applied to all trajectories, as already stated in Sect. 3.2 (similar as in Beuermann et al., 2002). For the RDF calculation, only advection and no mixing along the trajectories is assumed. In each time step of the RDF method, the ECMWF water vapor field is interpolated onto the locations of the trajectories and then projected onto the observed time-altitude grid of the GLORIA observations.

Figure 6 shows ECMWF water vapor mixing ratios five days prior to the measurement time as projected by the trajectories. The red boxes highlight the position of the water vapor filaments observed by GLORIA (see Fig. 3). With some small deviations in time and altitude, almost all of the observed filaments in the vortex can be reproduced by the RDF method. Note, that the RDF method cannot produce the effect of rehydration. This indicates that the water vapor filaments observed by GLORIA were not generated by rehydration, but are likely the signatures of moister air masses that were mixed into the vortex during the preceding 5 days. Continuing the RDF method further back in time, the filament 7 ($\approx$ 12 km) at 13:00 UTC emerges 35 days before observation and indicates the origin to be another mixing event. The time of in-mixing

ACPD
15, 7895–7932, 2015

CC BY

of the filament 7 was already visible in our analysis in Fig. 5. Thus, it seems that these filaments originate from several mixing events, not from a single mixing event only. Furthermore, very dry air masses observed in the time between 09:00 to 10:30 and 12:00 to 13:30 UTC down to 7 km (see Sect. 3.2) can also be partly reproduced with the RDF method, indicating that transport is the main reason for the occurrence of dry air below the thermal tropopause. The origin of these air masses and the transport mechanism are analyzed and discussed in the next subsection.

4.2.2 Transport of dehydrated air masses across the tropopause

The thermal tropopause in the Antarctic region is formed under unique climate conditions (Evtushevsky et al., 2011). The upper troposphere and lower stratosphere are generally very cold with a very weak vertical temperature gradient during winter and spring. Therefore, the thermal tropopause in the Antarctic region is rather poorly defined (Stohl and Sodemann, 2010). This is also implied by the tropopause heights derived from GLORIA, which have a broad scatter (± 0.5 km) at some places and indicate the weak vertical temperature gradient. In addition, the PV gradient at the transition between troposphere and stratosphere within the vortex (08:30–13:30 UTC) is small. The PV isolines (−4 and −2) in the vortex have a larger spacing than at the edge (jet region), where the vertical distance between the isolines decreases (08:15 and 13:30 UTC in Fig. 5). As a consequence, the tropopause and the PV gradient cannot serve as a strong transport barrier like they do in the mid-latitudes. Especially in the case of planetary wave breaking events that produce stratospheric intrusions, large amounts of air can be transported into the troposphere without strong resistance. Figure 7 shows the time difference between when each single trajectory from the GLORIA observation started and when the trajectory crossed the thermal tropopause from the stratosphere into the troposphere most recently in the past. This time is determined by counting the trajectory time steps backward in time to wherever the difference in altitude between current tropopause and trajectory is positive. Air parcels having stayed for the last 70 days within the troposphere (dark red colors) can clearly be assumed to be tropospheric nature.

The stratospheric and vortex air masses did not cross the tropopause (dark blue colors). The air masses below the measured tropopause are obviously more patchy and contain more trajectories originating from the troposphere (reddish colors). However, some freshly mixed in stratospheric air masses are also discernible below the thermal tropopause (light blue colors), down to 7 km. The green framed areas in Fig. 7 mark all the trajectories having tropopause crossing times between 0 and 70 days and where GLORIA observations reveal water vapor content of less than 3 ppmv. Indeed, there is a very good correlation between the light blue air masses, which crossed the tropopause between 2 and 6 days before, and the green framed areas marking the dehydrated air masses. In addition to the low water vapor content in the green framed areas, higher values of ozone were also observed by GLORIA, which reinforces the stratospheric origin of these air masses (not shown here).

Figure 8a and b shows the median potential temperature (theta) and altitude distributions of all trajectories within the green framed areas from Fig. 7 for the period of 5 months preceding (blue lines) and the first month following (red lines) the observation. The potential temperature is decreasing from about 380 to 310 K within five months, which reveals the well-known general descent of air masses in the polar vortex due to radiative cooling. After the trajectories have left the stratosphere and penetrated the troposphere, the general subsidence in the Antarctic troposphere caused by the katabatic surface winds leads to adiabatic heating of these air masses. Additionally, RWB events facilitate a wave-driven, secondary circulation that transports warmer air masses from around the vortex edge to the colder inner vortex. Despite the dryness of these air masses, the slight enhancement of ozone and the residual water vapor enable radiative cooling and a reduction in potential temperature i.e. descent of air masses continue down to 5 km altitude (300 K) in the time after the observation. Once transported into the troposphere, air masses will be transported down to near-surface level as suggested already by Roscoe (2004) and Stohl and Sodemann (2010).

ACPD
15, 7895–7932, 2015

CC BY

The point of in-mixing of stratospheric air masses into the troposphere and vice versa cannot be associated with a single event. In fact, successive Rossby wave activity at the vortex edge facilitates the transport process. If the isentropes cross the thermal tropopause (see Fig. 1b), and if the thermal tropopause is very weak at the lower border of the stratosphere, the tropopause is not able to prevent nearly vertical stratospheric/tropospheric exchange. This is a completely different situation compared to the subtropical jet, where the thermal tropopause and the PV gradient are typically strong enough to prevent such an exchange.

Here, strong Rossby wave activity is made visible by comparing the median latitude and equivalent latitude just a few days before the observation (6 to 17 September) as seen in Fig. 8c and d. The latitude is oscillating from near 60 down to 80° S, up to 55° S, and then back to 65° S, while the equivalent latitude in this time frame stays constant at around 70° S. This implies no PV change and only an isentropic latitudinal displacement due to planetary Rossby waves. Thus, Rossby wave breaking events drive the mixing process together with isentropic transport through the thermal tropopause.

Just in the middle of the time frame, on the point furthest south at latitudes around 80° S (see Fig. 8c) on the 9 September, the back trajectories split up into two different branches, indicating a bifurcation point (not shown here). This implies a mixing of air masses with different histories and also that this Rossby wave event is not the sole reason for the transport into the troposphere. Indeed, if one looks into the airmass history, additional Rossby wave events occurred in the days and weeks before. So it is not possible to match one specific event to the transport of all air masses which were observed below the tropopause with low water vapor content (green framed areas in Fig. 7). Also, the aforementioned filaments with enhanced water vapor in the vortex correspond to in-mixing due to the wave activity just 5 days before observations.

The vortex becomes more and more unstable during the Antarctic spring and one may assume that this in-mixing event is already a first sign of the vortex break-up. Haigh and Roscoe (2009) reported about recent Antarctic final warming events occurring between the beginning of December to late January at the 100 hPa level. Therefore,

ACPD
15, 7895–7932, 2015

the observed in-mixing of vortex air masses occurs long (at least two months) before the final warming and break-up of the vortex. It is therefore more or less independent of the final warming event and seems to be a usual process in the Antarctic winter and spring.

Finally, the reason for the large downward transport is a mixture of strong Rossby wave activity, the presence of a very weak thermal tropopause, which fails to act as a strong enough transport barrier, and the additional radiative cooling with corresponding subsidence of the air masses.

5 Conclusions

Detailed observations of dehydration and stratospheric/tropospheric exchange in the Antarctic UT/LS are very rare. In this study, high resolution in-situ measurements of strongly dehydrated air in the lower vortex with the hygrometers FISH and HAI are presented. The final dehydration can be traced back to several ice formation events, where water is sedimented out of the observed air masses. Dehydrated air masses are also observed with the high resolution remote sensing instrument GLORIA down to the thermal tropopause, as well as below this point, down to the free troposphere to 7 km in altitude. Besides dehydrated air masses, small filaments of enhanced water vapor are observed by GLORIA in the vortex air. These filaments can be clearly assigned to in-mixing of moister tropospheric air masses into the dry vortex at several points in time, indicating that this transport process occurs frequently.

With an extensive trajectory case study, dry air masses below the thermal tropopause are determined to have stratospheric origin. It is shown that these dry air masses are transported further down to near surface levels within one month. Both the in-mixing of moist tropospheric air into the stratosphere as well as the large-scale transport of dehydrated air masses into the troposphere confirm the ineffectiveness of the thermal tropopause as a transport barrier during Antarctic spring and winter (e.g. Roscoe, 2004; Evtushevsky et al., 2011). This transport is not caused by a single

ACPD
15, 7895–7932, 2015

CC BY

Rossby wave event, but rather the result of frequent in-mixing due to strong wave activity in combination with isentropes crossing the weak tropopause. Once the air masses have been transported into the troposphere, radiative cooling causes their subsidence to near surface levels around 5 km. The implication of frequent in-mixing of dry stratospheric air masses into the troposphere could on the one hand significantly reduce cloudiness and precipitation, and on the other hand increase ozone in the troposphere above Antarctica. In conclusion, frequent tropospheric/stratospheric intrusions can influence or be one cause of the unique Antarctic climate.

Acknowledgements. Sincere thanks goes to the whole CLaMS team and in particular to Jens-Uwe Grooß for supporting the trajectory calculations. We acknowledge the NASA Langley Research Atmospheric Science Data Center for providing the CALIPSO data. In addition, we acknowledge the European Centre for Medium-Range Weather Forecasts for meteorological reanalysis data support. The development and application of the HAI instrument was financially supported by the German science foundation DFG. We thank all members of the GLORIA instrument team for their great efforts in developing the first IR limb-imager. The GLORIA hardware was mainly funded by the Helmholtz Association of German Research Centers through several large investment funds. Great thanks goes to the coordinators of the TACTS campaign, Andreas Engel and Harald Bönisch, and to the coordinator of ESMVal campaign, Hans Schlager and of course to the whole HALO community for the great work during both campaigns. Finally, special thanks goes to Anna Luebke for language revision.

The article processing charges for this open-access publication have been covered by a Research Centre of the Helmholtz Association.

References

Beuermann, R., Konopka, P., Brunner, D., Bujok, O., Günther, G., McKenna, D. S., Lelieveld, J., Müller, R., and Schiller, C.: High-resolution measurements and simulation of stratospheric and tropospheric intrusions in the vicinity of the polar jet stream, Geophys. Res. Lett., 29, 1577, doi:10.1029/2001GL014162, 2002. 7913

CC BY

Buchholz, B.: Entwicklung, Primärvalidierung und Feldeinsatz neuartiger, kalibrierungsfreier Laser-Hygrometer für Forschungsflugzeuge, Dissertation, Technische Universität Darmstadt, 2014. 7902

Buchholz, B., Kühnreich, B., Smit, H. G. J., and Ebert, V.: Validation of an extractive, airborne, compact TDL spectrometer for atmospheric humidity sensing by blind intercomparison, Appl. Phys. B-Lasers O., 110, 249–262, doi:10.1007/s00340-012-5143-1, 2013. 7902

Buchholz, B., Böse, N., and Ebert, V.: Absolute validation of a diode laser hygrometer via intercomparison with the German national primary water vapor standard, Appl. Phys. B-Lasers O., 116, 883–899, doi:10.1007/s00340-014-5775-4, 2014. 7902

Dee, D. P., Uppala, S. M., Simmons, A. J., Berrisford, P., Poli, P., Kobayashi, S., Andrae, U., Balmaseda, M. A., Balsamo, G., Bauer, P., Bechtold, P., Beljaars, A. C. M., van de Berg, L., Bidlot, J., Bormann, N., Delsol, C., Dragani, R., Fuentes, M., Geer, A. J., Haimberger, L., Healy, S. B., Hersbach, H., Holm, E. V., Isaksen, L., Kallberg, P., Koehler, M., Matricardi, M., McNally, A. P., Monge-Sanz, B. M., Morcrette, J.-J., Park, B.-K., Peubey, C., de Rosnay, P., Tavolato, C., Thepaut, J.-N., and Vitart, F.: The ERA-Interim reanalysis: configuration and performance of the data assimilation system, Q. J. Roy. Meteor. Soc., 137, 553–597, doi:10.1002/qj.828, 2011. 7904, 7909

Ebert, V. and Wolfrum, J.: Absorption spectroscopy, in: Optical Measurements – Techniques and Applications (Heat and Mass Transfer), edited by: Mayinger, F. and Feldmann, O., 2nd ed., Springer Heidelberg, München, ISBN:978-3540666905, 273–312, 2000.

Engel, A., Bönisch, H., and TACTS-Team: An overview on the TACTS mission using the new German research aircraft HALO in summer 2012, EGU General Assembly, 15, EGU2013-25 9191, 07–12 April 2013, Vienna, Austria, 2013. 7899

Ern, M., Preusse, P., Gille, J. C., Hepplewhite, C. L., Mlynczak, M. G., Russell III, J. M., and Riese, M.: Implications for atmospheric dynamics derived from global observations of gravity wave momentum flux in stratosphere and mesosphere, J. Geophys. Res., 116, D19107, doi:10.1029/2011JD015821, 2011. 7911

Evtushevsky, O., Klekociuk, A., Grytsai, A., Milinevsky, G., and Lozitsky, V.: Troposphere and stratosphere influence on tropopause in the polar regions during winter and spring, Int. J. Remote Sens., 32, 3153–3164, doi:10.1080/01431161.2010.541515, 2011. 7914, 7917

Friedl-Vallon, F., Gulde, T., Hase, F., Kleinert, A., Kulessa, T., Maucher, G., Neubert, T., Olschewski, F., Piesch, C., Preusse, P., Rongen, H., Sartorius, C., Schneider, H., Schönfeld, A., Tan, V., Bayer, N., Blank, J., Dapp, R., Ebersoldt, A., Fischer, H., Graf, F., Guggen-

CC BY

moser, T., Höpfner, M., Kaufmann, M., Kretschmer, E., Latzko, T., Nordmeyer, H., Oelhaf, H., Orphal, J., Riese, M., Schardt, G., Schillings, J., Sha, M. K., Suminska-Ebersoldt, O., and Ungermann, J.: Instrument concept of the imaging Fourier transform spectrometer GLORIA, Atmos. Meas. Tech., 7, 3565–3577, doi:10.5194/amt-7-3565-2014, 2014. 7903

Giovanelli, G., Bortoli, D., Petritoli, A., Castelli, E., Kostadinov, I., Ravegnani, F., Redaelli, G., Volk, C. M., Cortesi, U., Bianchini, G., and Carli, B.: Stratospheric minor gas distribution over the Antarctic Peninsula during the APE-GAIA campaign, Int. J. Remote Sens., 26, 3343–3360, doi:10.1080/01431160500076210, 2005. 7898

Haigh, J. D. and Roscoe, H. K.: The final warming date of the Antarctic polar vortex and influences on its interannual variability, J. Climate, 22, 5809–5819, doi:10.1175/2009JCLI2865.1, 2009. 7916

Hoffmann, L., Xue, X., and Alexander, M. J.: A global view of stratospheric gravity wave hotspots located with Atmospheric Infrared Sounder observations, J. Geophys. Res., 118, 416–434, doi:10.1029/2012JD018658, 2013. 7911

James, P., Stohl, A., Forster, C., Eckhardt, S., Seibert, P., and Frank, A.: A 15-year climatology of stratosphere-troposphere exchange with a Lagrangian particle dispersion model – 2. Mean climate and seasonal variability, J. Geophys. Res., 108, 8522, doi:10.1029/2002JD002639, 2003. 7900

Jimenez, C., Pumphrey, H. C., MacKenzie, I. A., Manney, G. L., Santee, M. L., Schwartz, M. J., Harwood, R. S., and Waters, J. W.: EOS MLS observations of dehydration in the 2004–2005 polar winters, Geophys. Res. Lett., 33, L16806, doi:10.1029/2006GL025926, 2006. 7897, 7898, 7899

Kaufmann, M., Blank, J., Guggenmoser, T., Ungermann, J., Engel, A., Ern, M., Friedl-Vallon, F., Gerber, D., Grooß, J. U., Günther, G., Höpfner, M., Kleinert, A., Kretschmer, E., Latzko, Th., Maucher, G., Neubert, T., Nordmeyer, H., Oelhaf, H., Olschewski, F., Orphal, J., Preusse, P., Schlager, H., Schneider, H., Schuettemeyer, D., Stroh, F., Suminska-Ebersoldt, O., Vogel, B., M. Volk, C., Woiwode, W., and Riese, M.: Retrieval of three-dimensional small-scale structures in upper-tropospheric/lower-stratospheric composition as measured by GLORIA, Atmos. Meas. Tech., 8, 81–95, doi:10.5194/amt-8-81-2015, 2015. 7903

Kelly, K. K., Tuck, A. F., Murphy, D. M., Proffitt, M. H., Fahey, D. W., Jones, R. L., McKenna, D. S., Loewenstein, M., Podolske, J. R., Strahan, S. E., Ferry, G. V., Chan, K. R., Vedder, J. F., Gregory, G. L., Hypes, W. D., McCormick, M. P., Browell, E. V., and Heidt, L. E.: Dehydration

ACPD
15, 7895–7932, 2015

Transport of Antarctic dehydrated air into the troposphere

C. Rolf et al.

CC BY

in the lower Antarctic stratosphere during late winter and early spring, 1987, J. Geophys. Res., 94, 11317–11357, doi:10.1029/JD094iD09p11317, 1989. 7897

Khaykin, S. M., Engel, I., Vömel, H., Formanyuk, I. M., Kivi, R., Korshunov, L. I., Krämer, M., Lykov, A. D., Meier, S., Naebert, T., Pitts, M. C., Santee, M. L., Spelten, N., Wienhold, F. G., Yushkov, V. A., and Peter, T.: Arctic stratospheric dehydration – Part 1: Unprecedented observation of vertical redistribution of water, Atmos. Chem. Phys., 13, 11503–11517, doi:10.5194/acp-13-11503-2013, 2013. 7898, 7909

Khosrawi, F., Müller, R., Beuermann, J., Konopka, P., and Schiller, C.: Dehydration in the Northern Hemisphere mid-latitude tropopause region observed during STREAM 1998, Tellus B, 58, 206–217, doi:10.1111/j.1600-0889.2006.00182.x, 2006.

Khosrawi, F., Urban, J., Pitts, M. C., Voelger, P., Achtert, P., Kaphlanov, M., Santee, M. L., Manney, G. L., Murtagh, D., and Fricke, K.-H.: Denitrification and polar stratospheric cloud formation during the Arctic winter 2009/2010, Atmos. Chem. Phys., 11, 8471–8487, doi:10.5194/acp-11-8471-2011, 2011. 7898

Konopka, P., Günther, G., Müller, R., dos Santos, F. H. S., Schiller, C., Ravegnani, F., Ulanovsky, A., Schlager, H., Volk, C. M., Viciani, S., Pan, L. L., McKenna, D.-S., and Riese, M.: Contribution of mixing to upward transport across the tropical tropopause layer (TTL), Atmos. Chem. Phys., 7, 3285–3308, doi:10.5194/acp-7-3285-2007, 2007. 7909

Krautstrunk, M. and Giez, A.: The transition from FALCON to HALO era airborne atmospheric research, in: Atmospheric Physics, edited by: Schumann, U., Springer Berlin Heidelberg, 609–624, 2012. 7899

McKenna, D. S., Konopka, P., Grooss, J. U., Günther, G., Müller, R., Spang, R., Offermann, D., and Orsolini, Y.: A new Chemical Lagrangian Model of the Stratosphere (CLaMS) – 1. Formulation of advection and mixing, J. Geophys. Res., 107, 4309, doi:10.1029/2000JD000114, 2002. 7909

Meyer, J., Rolf, C., Schiller, C., Rohs, S., Spelten, N., Afchine, A., Zöger, M., Sitnikov, N., Thornberry, T. D., Rollins, A. W., Bozóki, Z., Tátrai, D., Ebert, V., Kühnreich, B., Mackrodt, P., Möhler, O., Saathoff, H., Rosenlof, K. H., and Krämer, M.: Two decades of water vapor measurements with the FISH fluorescence hygrometer: a review, Atmos. Chem. Phys. Discuss., 15, 7735–7782, doi:10.5194/acpd-15-7735-2015, 2015. 7901

Mihalikova, M. and Kirkwood, S.: Tropopause fold occurrence rates over the Antarctic station Troll (72° S, 2.5° E), Ann. Geophys., 31, 591–598, doi:10.5194/angeo-31-591-2013, 2013. 7900

ACPD
15, 7895–7932, 2015

CC BY

Müller, R. and Peter, T.: The Numerical Modeling of the Sedimentation of Polar Stratospheric Cloud Particles, Berichte der Bunsen-Gesellschaft-Physical Chemistry Chemical Physics, 96, Deut Bunsen Gesell Phys Chem, 353–361, 1992. 7910

Nash, E. R., Newman, P. A., Rosenfield, J. E., and Schoeberl, M. R.: An objective determination of the polar vortex using Ertel's potential vorticity, J. Geophys. Res., 101, 9471–9478, doi:10.1029/96JD00066, 1996. 7905, 7912, 7925

Ndarana, T., Waugh, D. W., Polvani, L. M., Correa, G. J. P., and Gerber, E. P.: Antarctic ozone depletion and trends in tropopause Rossby wave breaking, Atmos. Sci. Lett., 13, 164–168, doi:10.1002/asl.384, 2012. 7900

Nedoluha, G. E., Bevilacqua, R. M., and Hoppel, K. W.: POAM III measurements of dehydration in the Antarctic and comparisons with the Arctic, J. Geophys. Res., 107, 8290, doi:10.1029/2001JD001184, 2002. 7897, 7898, 7899, 7910, 7911

Nedoluha, G. E., Benson, C. M., Hoppel, K. W., Alfred, J., Bevilacqua, R. M., and Drdla, K.: Antarctic dehydration 1998–2003: Polar ozone and aerosol measurement III (POAM) measurements and integrated microphysics and aerosol chemistry on trajectories (IMPACT) results with four meteorological models, J. Geophys. Res., 112, D07305, doi:10.1029/2006JD007414, 2007. 7898

Pitts, M. C., Poole, L. R., and Thomason, L. W.: CALIPSO polar stratospheric cloud observations: second-generation detection algorithm and composition discrimination, Atmos. Chem. Phys., 9, 7577–7589, doi:10.5194/acp-9-7577-2009, 2009. 7904

Pitts, M. C., Poole, L. R., Dörnbrack, A., and Thomason, L. W.: The 2009–2010 Arctic polar stratospheric cloud season: a CALIPSO perspective, Atmos. Chem. Phys., 11, 2161–2177, doi:10.5194/acp-11-2161-2011, 2011. 7904

Ploeger, F., Konopka, P., Günther, G., Grooss, J.-U., and Müller, R.: Impact of the vertical velocity scheme on modeling transport in the tropical tropopause layer, J. Geophys. Res., 115, D03301, doi:10.1029/2009JD012023, 2010. 7909

Riese, M., Oelhaf, H., Preusse, P., Blank, J., Ern, M., Friedl-Vallon, F., Fischer, H., Guggenmoser, T., Höpfner, M., Hoor, P., Kaufmann, M., Orphal, J., Plöger, F., Spang, R., Suminska-Ebersoldt, O., Ungermann, J., Vogel, B., and Woiwode, W.: Gimballed Limb Observer for Radiance Imaging of the Atmosphere (GLORIA) scientific objectives, Atmos. Meas. Tech., 7, 1915–1928, doi:10.5194/amt-7-1915-2014, 2014. 7903

Roscoe, H. K.: Possible descent across the "Tropopause" in Antarctic winter, Adv. Space Res., 33, 1048–1052, doi:10.1016/S0273-1177(03)00587-8, 2004. 7900, 7915, 7917

cc BY

Schiller, C., Bauer, R., Cairo, F., Deshler, T., Dornbrack, A., Elkins, J., Engel, A., Flentje, H., Larsen, N., Levin, I., Müller, M., Oltmans, S., Ovarlez, H., Ovarlez, J., Schreiner, J., Stroh, F., Voigt, C., and Vömel, H.: Dehydration in the Arctic stratosphere during the SOLVE/THESEO-2000 campaigns, J. Geophys. Res., 107, 8293, doi:10.1029/2001JD000463, 2002. 7898

Schlager, H.: ESMval (Earth System Model Validation), available at: http://www.pa.op.dlr.de/ESMVal, last access: 18 July 2014. 7898

Schoeberl, M. R. and Dessler, A. E.: Dehydration of the stratosphere, Atmos. Chem. Phys., 11, 8433–8446, doi:10.5194/acp-11-8433-2011, 2011. 7898, 7899

Schoeberl, M. R., Lait, L. R., Newman, P. A., and Rosenfield, J. E.: The structure of the polar vortex, J. Geophys. Res., 97, 7859–7882, 1992. 7897, 7899

Solomon, S.: Stratospheric ozone depletion: a review of concepts and history, Rev. Geophys., 37, 275–316, doi:10.1029/1999RG900008, 1999. 7898

Stohl, A. and Sodemann, H.: Characteristics of atmospheric transport into the Antarctic troposphere, J. Geophys. Res., 115, D02305, doi:10.1029/2009JD012536, 2010. 7900, 7911, 7914, 7915

Tuck, A. F., Watson, R. T., Condon, E. P., Margitan, J. J., and Toon, O. B.: The planning and execution of Er-2 and Dc-8 aircraft flights over Antarctica, August and September 1987, J. Geophys. Res., 94, 11181–11222, doi:10.1029/JD094iD09p11181, 1989. 7898

Tuck, A. F., Brune, W. H., and Hipskind, R. S.: Airborne Southern Hemisphere Ozone Experiment Measurements for Assessing the Effects of Stratospheric Aircraft (ASHOE/MAESA): a road map, J. Geophys. Res., 102, 3901–3904, doi:10.1029/96JD02745, 1997. 7898

Ungermann, J., Blank, J., Lotz, J., Leppkes, K., Hoffmann, L., Guggenmoser, T., Kaufmann, M., Preusse, P., Naumann, U., and Riese, M.: A 3-D tomographic retrieval approach with advection compensation for the air-borne limb-imager GLORIA, Atmos. Meas. Tech., 4, 2509–2529, doi:10.5194/amt-4-2509-2011, 2011. 7903

Ungermann, J., Blank, J., Dick, M., Ebersoldt, A., Friedl-Vallon, F., Giez, A., Guggenmoser, T., Höpfner, M., Jurkat, T., Kaufmann, M., Kaufmann, S., Kleinert, A., Krämer, M., Latzko, T., Oelhaf, H., Olchewski, F., Preusse, P., Rolf, C., Schillings, J., Suminska-Ebersoldt, O., Tan, V., Thomas, N., Voigt, C., Zahn, A., Zöger, M., and Riese, M.: Level 2 processing for the imaging Fourier transform spectrometer GLORIA: derivation and validation of temperature and trace gas volume mixing ratios from calibrated dynamics mode spectra, Atmos. Meas. Tech. Discuss., 7, 12037–12080, doi:10.5194/amtd-7-12037-2014, 2014. 7904

ACPD
15, 7895–7932, 2015

Transport of Antarctic dehydrated air into the troposphere

C. Rolf et al.

CC BY

van de Berg, W. J., van den Broeke, M. R., and van Meijgaard, E.: Heat budget of the East Antarctic lower atmosphere derived from a regional atmospheric climate model, J. Geophys. Res., 112, D23101, doi:10.1029/2007JD008613, 2007. 7900

Vömel, H., Oltmans, S. J., Hofmann, D. J., Deshler, T., and Rosen, J. M.: The evolution of the dehydration in the Antarctic stratospheric vortex, J. Geophys. Res., 100, 13919–13926, doi:10.1029/95JD01000, 1995. 7897, 7898

Zahn, A., Weppner, J., Widmann, H., Schlote-Holubek, K., Burger, B., Kühner, T., and Franke, H.: A fast and precise chemiluminescence ozone detector for eddy flux and airborne application, Atmos. Meas. Tech., 5, 363–375, doi:10.5194/amt-5-363-2012, 2012. 7903

Zöger, M., Afchine, A., Eicke, N., Gerhards, M. T., Klein, E., McKenna, D. S., Morschel, U., Schmidt, U., Tan, V., Tuitjer, F., Woyke, T., and Schiller, C.: Fast in situ stratospheric hygrometers: A new family of balloon-borne and airborne Lyman alpha photofragment fluorescence hygrometers, J. Geophys. Res., 104, 1807–1816, doi:10.1029/1998JD100025, 1999. 7901

CC BY

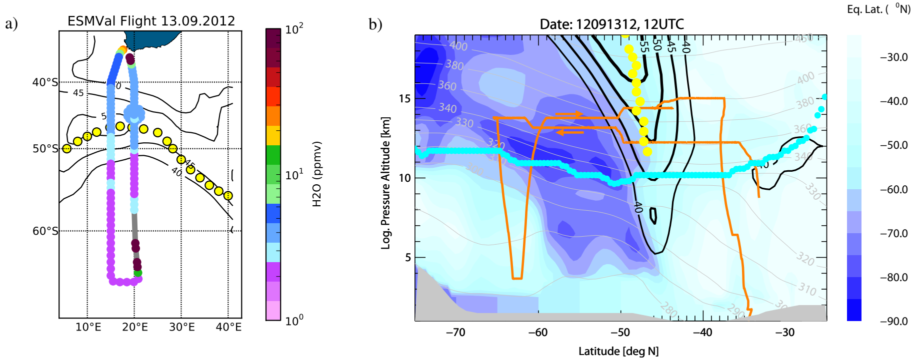

Figure 1. Flight pattern of the ESMVal flight on 13 September 2012. The black contours illustrate the horizontal westerly wind from ECMWF data. Yellow dots represent the vortex edge derived from the Nash criterion (Nash et al., 1996) based on ECMWF data. **(a)** Horizontal map of water vapor mixing ratios measured by FISH (5 min averaged data) is color coded on the flight path (gray color indicate data gaps due to the dive). **(b)** Meridional cross-section of equivalent latitude along the flight path (orange line) calculated from ECMWF data. Blue dots represent the ECMWF thermal tropopause.

ACPD
15, 7895–7932, 2015

CC BY

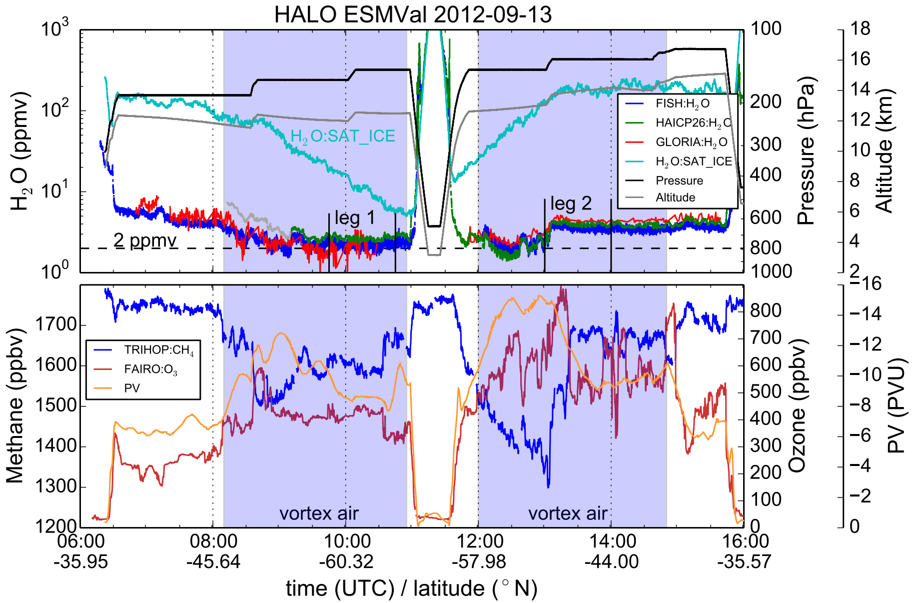

Figure 2. Timeseries of ESMVal Antarctica flight on 13 September 2012: the upper panel shows FISH (blue), HAI (green) and GLORIA (red) water vapor measurements, water vapor saturation mixing ratio with respect to ice (cyan, derived from HALO temperature), pressure (black), and altitude (gray) at flight level. The lower panel shows the tracer observations ozone (red), and methane (blue) and interpolated ECMWF PV values (orange). Time ranges within the vortex are marked with bluish shadows according to the tracer measurements. Time ranges leg 1 and leg 2 are marked for hygrometer intercomparison of FISH and HAI (see text).

ACPD
15, 7895–7932, 2015

Transport of Antarctic dehydrated air into the troposphere

C. Rolf et al.

CC BY

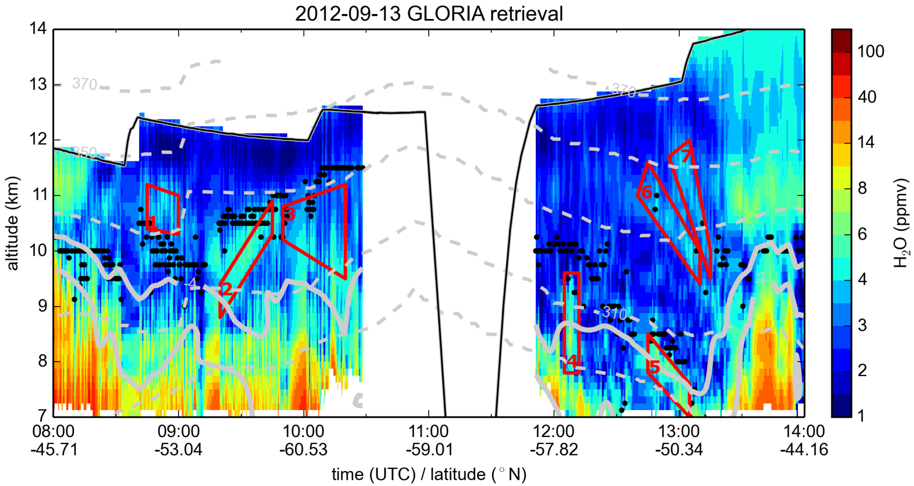

Figure 3. GLORIA time series of the H_2O retrieval product (13 September 2012). The solid black line and the black dots represent the flight path and thermal tropopause derived from the GLORIA temperature measurements, respectively. The dashed gray lines and the solid lines marks isolines of potential temperature (290–370 K, $\Delta\theta = 20$ K) and PV (−2 and −4 PVU), respectively. The red boxes marks filaments (1–7) with slightly enhanced water vapor mixing ratios in or below the vortex.

ACPD
15, 7895–7932, 2015

Transport of Antarctic dehydrated air into the troposphere

C. Rolf et al.

Title Page
Abstract Introduction
Conclusions References
Tables Figures
◀I ▶I
◀ ▶
Back Close
Full Screen / Esc
Printer-friendly Version
Interactive Discussion

CC BY

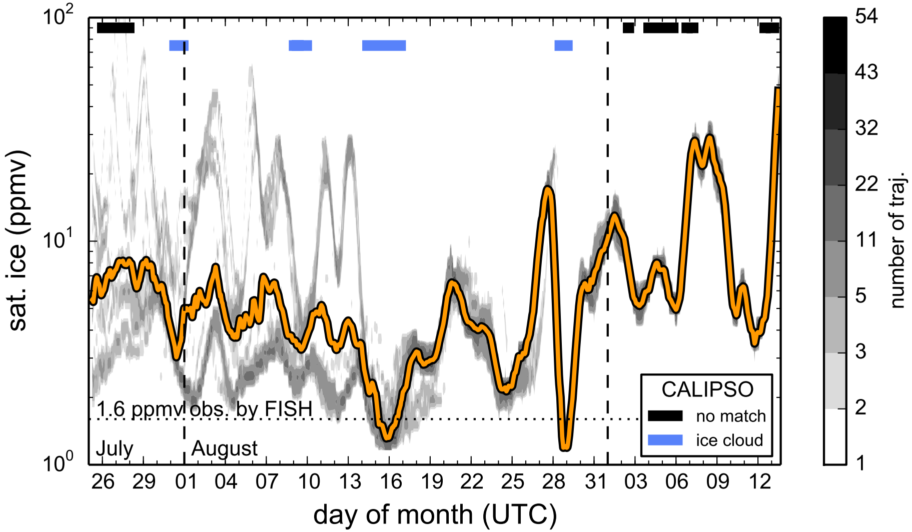

Figure 4. Calculated frequency distribution (number, gray shadow) and median (orange line) of ice saturation mixing ratio along trajectories 50 days back in time starting at the flight path on 13 September 2012 (12:20 to 12:29 UTC, 54 trajectories in total). If more than 50 % of trajectories have a corresponding CALIPSO observations of ice or no ice, the time is marked with blue or white, respectively. Otherwise, it is marked in black, indicating no CALIPSO match.

ACPD
15, 7895–7932, 2015

Transport of Antarctic dehydrated air into the troposphere

C. Rolf et al.

Title Page
Abstract Introduction
Conclusions References
Tables Figures
◀ ▶
Back Close
Full Screen / Esc
Printer-friendly Version
Interactive Discussion

CC BY

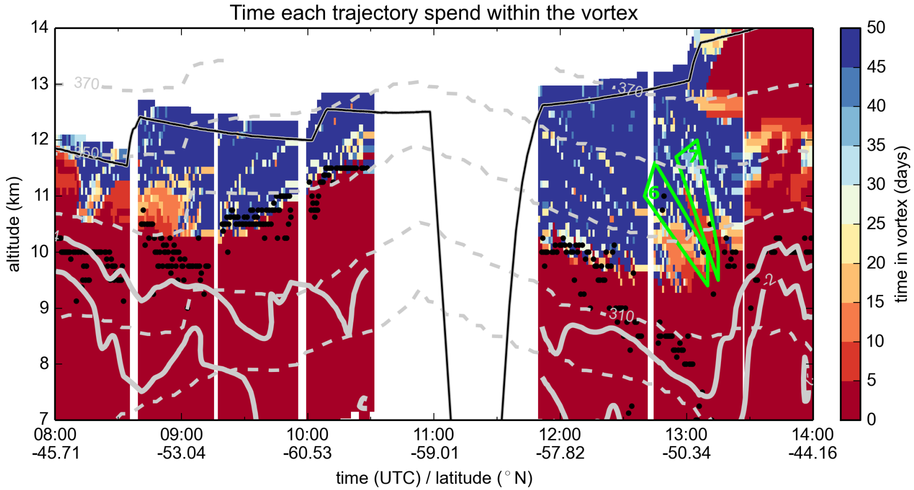

Figure 5. The time each GLORIA tangent point trajectory has spent in the vortex before the measurement. The green boxes mark two of the filaments (6, 7) observed by GLORIA (see Fig. 3). The flight path, tropopause height, potential temperature, and PV isolines are the same as in Fig. 3.

ACPD
15, 7895–7932, 2015

Transport of Antarctic dehydrated air into the troposphere

C. Rolf et al.

CC BY

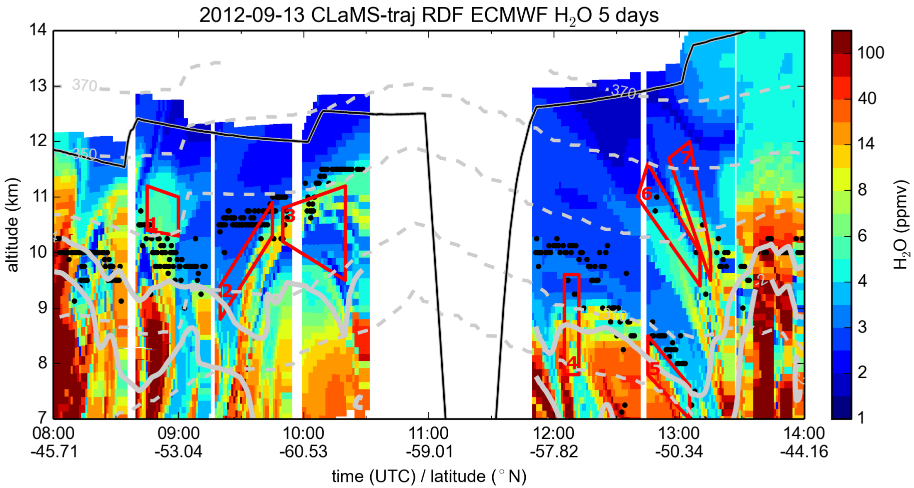

Figure 6. RDF (Reverse Domain Filling) of each GLORIA tangent point trajectory with ECMWF water vapor of 5 days prior the measurement time. Red boxes show the location of the observed filaments. The flight path, tropopause height, potential temperature, and PV isolines are the same as in Fig. 3.

ACPD
15, 7895–7932, 2015

Transport of Antarctic dehydrated air into the troposphere

C. Rolf et al.

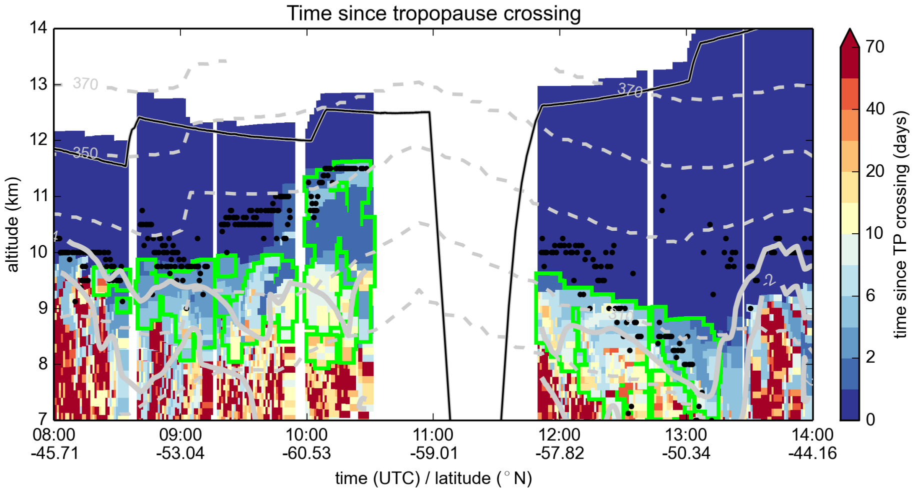

Figure 7. The color code denotes the time since trajectories passed the thermal tropopause from stratosphere to troposphere. Bluish colors denote trajectories which recently passed the thermal tropopause, reddish colors indicate tropopause crossings longer ago. The green framed areas mark the trajectories where GLORIA observations show water vapor below 3 ppmv. The flight path, tropopause height, potential temperature, and PV isolines are the same as in Fig. 3.

ACPD
15, 7895–7932, 2015

cc BY

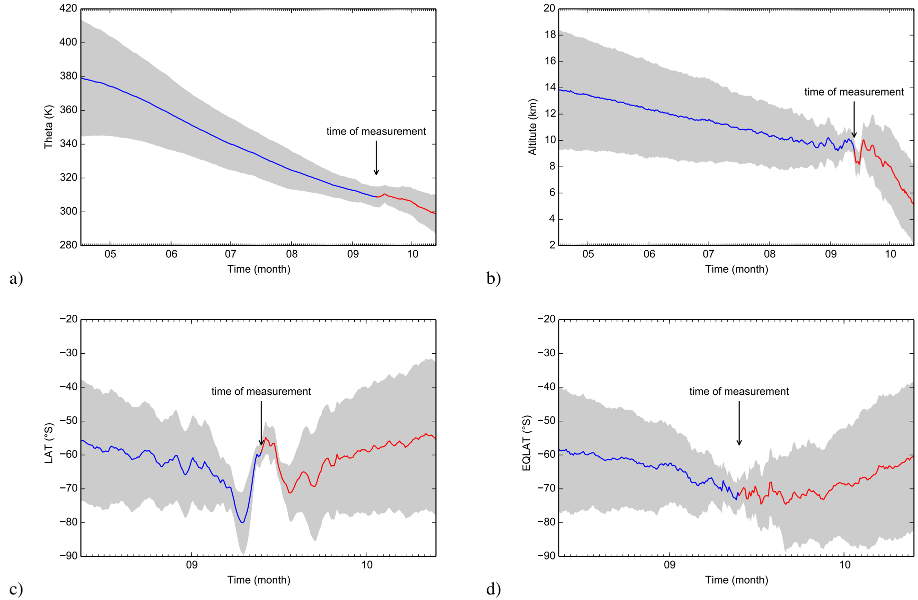

Figure 8. Air parcel properties based on trajectory analyses for all green framed trajectories from Fig. 7 for the period of 5 months before (blue lines) to 1 month after the measurement (red lines): **(a)** median of potential temperature (theta), **(b)** median altitude above mean sea level, **(c)** median latitude from 1 month before to 1 month after observation, **(d)** median equivalent latitude from 1 month before to 1 month after observation. The gray shaded areas marks the SD of the 1400 trajectories.

ACPD
15, 7895–7932, 2015

Transport of Antarctic dehydrated air into the troposphere

C. Rolf et al.

CC BY